Dendritic action potentials and computation in human layer 2/3 cortical neurons

5

Short title: Dendritic spikes in humans cortical neurons

Albert Gidon[1], Timothy Adam Zolnik[1], Pawel Fidzinski[2], Felix Bolduan[3], Athanasia Papoutsi[4], Panayiota Poirazi[4], Martin Holtkamp[2], Imre Vida[3,5], Matthew Evan Larkum[1*]

10

[1] Institute for Biology, Humboldt-Universität zu Berlin, Berlin, Germany.

[2] Epilepsy-Center Berlin-Brandenburg, Department of Neurology, Charité - Universitätsmedizin Berlin, Germany.

[3] Institute of Integrative Neuroanatomy, Charité-Universitätsmedizin Berlin, Berlin, Germany.

15 [4] Institute of Molecular Biology and Biotechnology-Foundation for Research and Technology Hellas (IMBB-FORTH), Crete, Greece.

[5] NeuroCure Cluster, Charité - Universitätsmedizin Berlin, Germany.

*Corresponding author E-mail: matthew.larkum@hu-berlin.de

20

The active electrical properties of dendrites shape the neuronal input/output and are fundamental to brain function. Our knowledge of active dendrites has been almost entirely acquired from rodents. Here we investigated the dendrites of layer 2/3 neurons of the human cerebral cortex *ex vivo*. In these neurons, we discovered a class of calcium-mediated dendritic action potentials (dCaAPs) whose waveform and effects on neuronal output have not previously been described. In contrast to typical "all-or-none" action potentials, dCaAPs were graded; their amplitudes were maximal for threshold-level stimuli but dampened for stronger stimuli. These dCaAPs enabled the dendrites of individual human neocortical pyramidal neurons to classify linearly non-separable inputs, a computation conventionally thought to require multi-layered networks.

5

10

One Sentence Summary: Newly discovered dendritic action potentials extend the repertoire of computations available to human neurons

The expansion of the human brain during evolution led to an extraordinarily thick cortex (~3 mm), which is disproportionately thickened in layer 2 and 3 (L2/3) (*1*). Consequently, human cortical neurons of L2/3 comprise large and elaborate dendritic trees (*2, 3*) decorated by numerous synaptic inputs (*1*). The active electrical properties of these dendrites largely determine the repertoire of transformations of the synaptic inputs to axonal action potentials (APs) at the output and thus, constitute a key element of the neuron's computational power.

We used dual somato-dendritic patch clamp and two-photon imaging to directly investigate the active properties of L2/3 dendrites in acute slices from surgically resected brain tissue of the human neocortex in epilepsy and tumor patients. Subthreshold (steady-state) potentials attenuated from the dendrite to the soma with a length constant (λ_{steady}) of 195 μm (**Fig. S1;** $n = 23$). In the opposite direction, the back-propagating action potentials (bAPs) attenuated from the soma to the dendrite with λ_{bAP} of 290 μm (**Fig. 1**A–C; $n = 31$). Both λ_{bAP} and λ_{steady} were shorter than the length of the apical dendrite (somata of these cells were located ~850 μm below the pia mater, on average, and the apical dendrite extended up to layer 1) implying that strong attenuation governs the electrical activity to and from most synapses located on the apical dendrite.

We filled cells with the calcium indicator Oregon-green BAPTA (100 μM) and measured the change in fluorescence ($\Delta F/F$) under a 2-photon microscope while triggering APs at the soma. Trains of somatic APs (10 APs) at 50 Hz failed to cause Ca^{2+} influx at distal apical dendrites (**Fig. S2**). AP trains with a higher frequency (10 APs at 200 Hz) did invade most of the apical dendrite similarly to what has been shown previously in rodents L2/3 pyramidal neurons (*4*). However, these high frequency signals were substantially attenuated at distal tuft dendrites (**Fig.**

S2). Furthermore, Ca^{2+} influx in spines was similar to the nearby dendritic branches, regardless of the somatic AP frequency (**Fig. S2**D).

We next examined whether human L2/3 dendrites have intrinsic mechanisms to compensate for the large dendritic attenuation. We injected a current step into the dendrite (I_{dend}) and recorded the membrane potentials at both the dendrite and at the soma. At the soma and at the proximal dendritic sites (170 μm from the soma on average), a suprathreshold current readily evoked somatic APs which back propagated into the dendrite (**Fig. 1**A,B, **Fig. S5**H). However, when the dendritic electrode was positioned more distally, suprathreshold stimuli often evoked trains of repetitive action potentials that were initiated exclusively in the dendrite (**Fig. 1**D, for transient stimulus see **Fig. S10**). These results imply that L2/3 dendrites in human cortical pyramidal neurons are distinctly more excitable than the homologues dendrites in rodents where similar steady currents evoke, at most, only a single dendritic AP at the beginning of the voltage response (*5*). In contrast to L2/3 pyramidal neurons, layer 5 pyramidal neurons of the human neocortex were recently reported to have reduced dendritic excitability as compared with their homologue neurons in rodents (*6*).

High frequency dendritic APs (>200 Hz) that were uncoupled from somatic firing have been observed in rodent dendrites *in vivo* (*7, 8*). The authors of these studies attributed these spikes to dendritic voltage-gated Na^+ channels and/or NMDA receptors. The dendritic APs in human L2/3 neurons were not blocked by the sodium channel blocker TTX (1 μM; *n* = 4 cells; **Fig. S3**) but were abolished by the Ca^{2+} channel blocker Cd^{2+} (200 μM; *n* = 5 cells; **Fig. S3**). The dendritic Ca^{2+} APs we observed in human L2/3 have not been described in cortical neurons of other mammalian species. Dendritic sodium APs (or assumed as such) in rodents' neurons have been variously named dendritic spikes (*9*), prepotentials (*10*), Na-dSpikes (*11*) and dendritic action

potentials (DAPs) (*8*). To distinguish the dendritic APs we found in the human dendrites from those described previously, we refer to them as dendritic Ca^{2+} APs (dCaAPs).

dCaAPs were present not only in neurons from the temporal lobe of epilepsy patients but also in neurons from other neocortical areas of tumor patients (*n* = 4 cells from 3 patients; **Fig. S4**), suggesting that dCaAPs are neither regionally confined nor related to pathology.

dCaAPs waveform was stereotypical and easily distinguished from bAPs. dCaAPs were typically wider than bAPs (width of 4.4 ± 1.4 ms, range between 2.6 and 8.0 ms; *n* = 32), were slow-rising, and did not have a kink at onset (*7*) (**Fig. 1**D). The majority (27 out of 39) of the cells showed a train of (two or more) dCaAPs with mean firing rate of 4.6 ± 1.7 Hz (dCaAPs/sec). In the remaining 12 dendrites, a single dCaAP was triggered immediately after beginning of the stimulus. Unlike the bAP (**Fig. 1C**), the amplitude of the dCaAPs (43.8 ± 13.8 mV, range between 13.0 and 67.0 mV; *n* = 32; measured at threshold; **Fig. 1E**) and their upstroke (**Fig. S5**) were not dependent on the distance from the soma which is consistent with both variability of the dCaAP initiation site and variability of dCaAP properties (for further details see **Figs. S5** and **S11)**. We never detected high-amplitude, long-duration, Ca^{2+} mediated plateau potentials which are common in the apical dendrites of L5 neurons in rodents.

The impact of dCaAPs on the soma was variable. In some of the cells (17/37 cells), the dCaAPs were coupled with somatic APs ("coupled" dCaAPs; e.g. **Fig. 1**F). Unlike forward propagating dendritic APs in other pyramidal neurons (*12–14*), coupled dCaAPs triggered somatic APs immediately and/or with a delay ranging between 21.6 and 116.9 ms (53.8 ± 26.8 ms on average in 11 out of 17 coupled cells; **Fig. 1**F,G and **Fig. S6**). Coupled dCaAPs that triggered somatic AP with a delay where classified as "complex". Without exception, each coupled dCaAP triggered a single somatic AP implying that unlike calcium APs in the dendrites of other neurons (*15, 16*),

dCaAPs did not induce bursts of somatic APs. In the other 20 cells, dCaAPs were uncoupled. They were confined to the apical dendrite, unable to evoke somatic APs. Typically, uncoupled dCaAPs were observed in more distal dendritic recording sites (335 ± 113 μm from the soma) than the coupled dCaAPs that triggered somatic APs (265 ± 71 μm from the soma) but the distance difference was not statistically significant (Wilcoxon rank-sum test, $p = 0.077$). Additionally, one coupled and three uncoupled cells fired bursts of three or more dCaAPs at the beginning of the stimulus ($28 - 73$ Hz).

In **Fig. S7,** we summarize the classification of the dCaAPs based on their ability to trigger APs at the soma (i.e. "coupled" vs. "uncoupled") and their complexity (i.e. "complex" and/or "simple"). Most of the dendrites with complex dCaAPs also triggered simple dCaAPs, suggesting that their behavior might be activity or input dependent and/or modulated by other factors (e.g. *17*).

dCaAPs affected the input/output transformation of the cells. Typically, somatic AP firing increases with the input current intensity injected to the soma. In contrast, in 4 cells (out of 12 cells that had repetitive and coupled dCaAPs) our recordings revealed an inverse behavior where increasing the intensity of dendritic (rather than somatic) current injection resulted in decreased somatic firing. For example, in **Fig. 2**A,B the dendritic electrode evoked 1 or 2 somatic APs with current near threshold but failed to evoke APs for larger current intensity. In contrast, at the soma of the same cells, AP output increased with the inputs strength (**Fig. 2**C). These results are explained by the unusual active properties of dCaAPs. dCaAPs evoked by the dendritic electrode, triggered somatic APs near threshold but were suppressed by further increase in the stimulus intensity (**Fig. 2**B).

The dendritic activation function (namely, the amplitude of dCaAPs as a function of the intensity of the current injection in the dendrite, I_{dend}) reached its maximal value at rheobase (i.e. for

$I_{dend} = I_{rhe}$ where I_{rhe} is the threshold current for triggering a dCaAP) and decayed for stronger I_{dend} (**Fig. 2**D–F, 12 uncoupled dCaAPs). The mean width of the dendritic activation function (defined here as the decay constant of a single exponential fit) was 0.39 (0.38 median; in units of I_{rhe}), indicating that dCaAPs are sharply tuned (highly selective) to a particular input strength. Additionally, L2/3 dendrites were heterogeneous in their activation function threshold and width (**Fig. 2**F). In contrast, in a similar range of input intensities somatic APs (**Fig. 2**G-H) showed a typical threshold activation function; once a somatic AP was triggered, its amplitude was virtually independent of the input intensity (**Fig. 2**H). Unlike other dendritic APs in the mammalian neocortex, namely, NMDA spikes (*18*) and dendritic Ca^{2+} APs in layer 5 pyramidal neurons (*15, 19–22*) that were previously shown to increase with the stimulus strength, the activation function of dCaAPs in L2/3 neurons was sharply tuned to a specific input strength (**Fig. 2**I).

We used a compartmental model of a L2/3 pyramidal neuron that replicated the phenomenology of the dCaAP behavior in the dendrite in order to investigate the functional outcome of the dCaAP activation function (for a biophysical model of dCaAPs see **Fig. S12**). L2/3 pyramidal neuron morphology was digitally reconstructed and modeled in the NEURON (*23*) simulation environment (**Fig. 3**A). The dCaAP's threshold, width, and amplitude as a function of the input strength were simulated by sum of current sources with a sigmoidal shape (for details see **Methods** and **Fig. 3**A right panel). To simulate two distinct classes of inputs, pathways *X* and *Y*, we used 25 excitatory synapses for each pathway (**Fig. 3**A) targeting a subregion of the apical dendrite (blue and red dots in **Fig. 3**A). Each of these pathways was able to trigger dCaAPs by itself (**Fig. 3**B,C). Due to the activation function of the dCaAPs in our simulation, coincident activation of two synaptic input pathways diminished the dCaAP amplitude (**Fig. 3**D) in contrast

to other dendritic APs that amplify coincident dendritic inputs (*24*), e.g., in layer 5 pyramidal neurons in the rodent neocortex (*25*) or in CA1 neurons of the rodent hippocampus (*26*). Our simulation is therefore a simple and explicit demonstration of how the dendritic mechanism observed in human L2/3 pyramidal neurons computes an anti-coincident function for multiple input pathways, limiting the number and/or strength of inputs integrated in the dendrite (for impact on the cell body see **Fig. S9**). Inhibition (*27, 28*) placed at the same dendritic subregion (20 GABAergic synapses), in addition to the two excitatory pathways, repolarized the membrane and recovered the amplitude of the dCaAPs (**Fig. 3**E; cf. *29*). These results suggest that the precise balance between excitation and inhibition is essential for the generation of dCaAPs and indicate a counter-intuitive role for inhibition in enhancing the excitability of the dendrite (see also **Fig. S9**C,D).

It has long been assumed that the summation of excitatory synaptic inputs at the dendrite and the output at the axon can only instantiate logical operations such as AND and OR (*30*). Traditionally, the XOR operation has been thought to require a network solution (*31, 32*). We found that the dCaAP's activation function allowed them to effectively compute the XOR operation in the dendrite by suppressing the amplitude of the dCaAP when the input is above the optimal strength (**Fig. 2**). Thus, based on our results and others (*30, 33*), in **Fig. 3**F,G we consider a model that portrays the somatic and dendritic compartments of L2/3 neuron as a network of coupled logical operators and corresponding activation functions. In this model, XOR operation is performed in the dendrites with dCaAPs, whereas AND/OR operations are performed at the soma and tuft/basal dendrites with sodium and NMDA spikes, respectively (*20, 25, 34, 35*). Our findings provide insights into the physiological building blocks that constitute the algorithms of cellular function, which ultimately give rise to the cortical network behavior.

Author contributions: M.E.L. and A.G. conceptualized and performed the experiments and analysis and wrote the original draft. T.A.Z. performed the 2-p experiments. P.F. and M.H. managed human tissue ethical aspects, delivery, and quality optimization. A.G., A.P., and P.P. conceptualized and created the models. F.B. and I.V. performed visualization, imaging, and morphological reconstruction of recorded neurons. All the authors participated in writing, reviewing, and editing the manuscript.

Competing interests: Authors declare no competing interests.

Data and materials availability:
NEURON simulation files are available at http://modeldb.yale.edu/254217 for Fig. 3 and S9 and at http://modeldb.yale.edu/260178 for Fig. S12. Reconstructed neurons and all summary graphs with corresponding data are stored at https://zenodo.org, DOI: 10.5281/zenodo.3530043.

Supplementary Materials:

Materials and Methods

Figures S1–S12
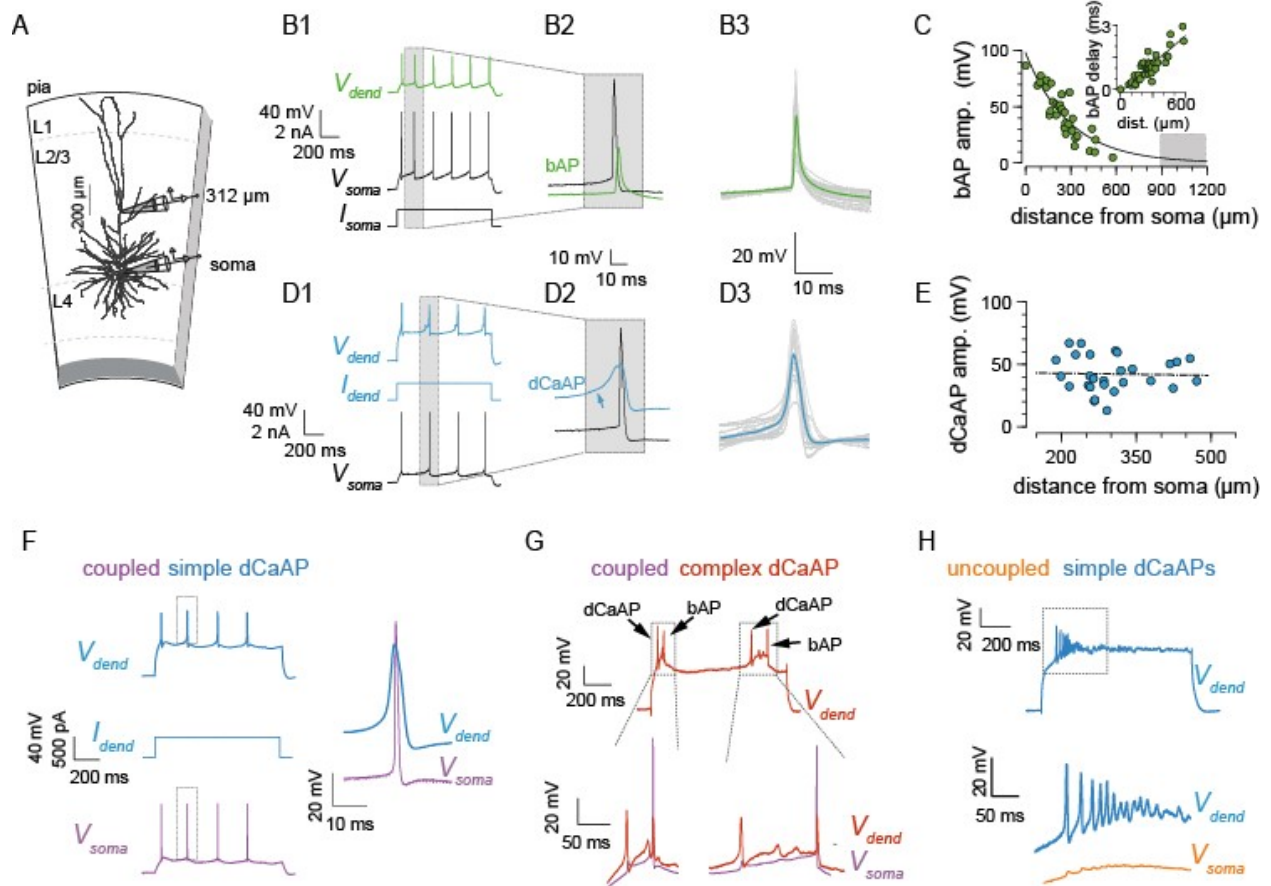
Tables S1, S2

References (*36–50*)

Fig. 1. Back-propagating action potentials (bAPs) and dendritic Ca^{2+} action potentials (dCaAPs) in human dendrites of L2/3 neurons.

A. Experimental setting: layer 2/3 neuron at a depth of 1130 μm below the pial surface with a somatic electrode and a dendritic electrode placed at 312 μm from the soma. **B1.** Recordings from the cell in A. bAPs in green (V_{dend}) and corresponding somatic APs in black (V_{soma}) triggered by somatic current injection (I_{soma}). **B2**. Somatic AP preceded the bAP (magnified from the frame in B1). **B3.** bAPs in 16 dendrites (gray) and their average (green) aligned to their peak. **C.** bAP amplitude (green dots) and exponential fit (length constant λ_{bAP}= 290 μm; $n = 31$; dashed line) against distance from the soma. Gray area indicates the putative tuft region in layer 1 for the longest dendrite. Inset. Delay of the bAP peak against distant from the soma with linear fit ($r^2 = 0.78$). **D1.** dCaAPs (V_{dend}; blue) triggered by a square current injected at the dendrite (I_{dend}) and the resulting somatic AP (black) from the cell in A. **D2.** Somatic AP (in black) and a dCaAP (in blue) magnified from D1. The slow rising dCaAP (blue arrow) precedes the somatic AP. **D3.** Initial dCaAP in each recording at threshold in the same 16 dendrites (gray) in B3 and their average trace (blue) aligned to their peak. **E.** dCaAP amplitude is independent of the distance from the soma ($n = 28$ cells). Linear fit in dashed line ($r^2 = 0.0009$). **F.** *Left*, "coupled" and "simple" dCaAPs (blue trace) and somatic APs (violet trace) triggered by I_{dend}. *Right*, Magnified dCaAP (in blue) and a somatic AP (in violet) framed in the traces on the left. **G.** *Top*. Two "Coupled" and "complex" dCaAPs (in red) triggered delayed somatic APs (in violet magnified at the bottom). **H.** Burst of "simple" and "uncoupled" dCaAPs in blue (top) with somatic APs (bottom).
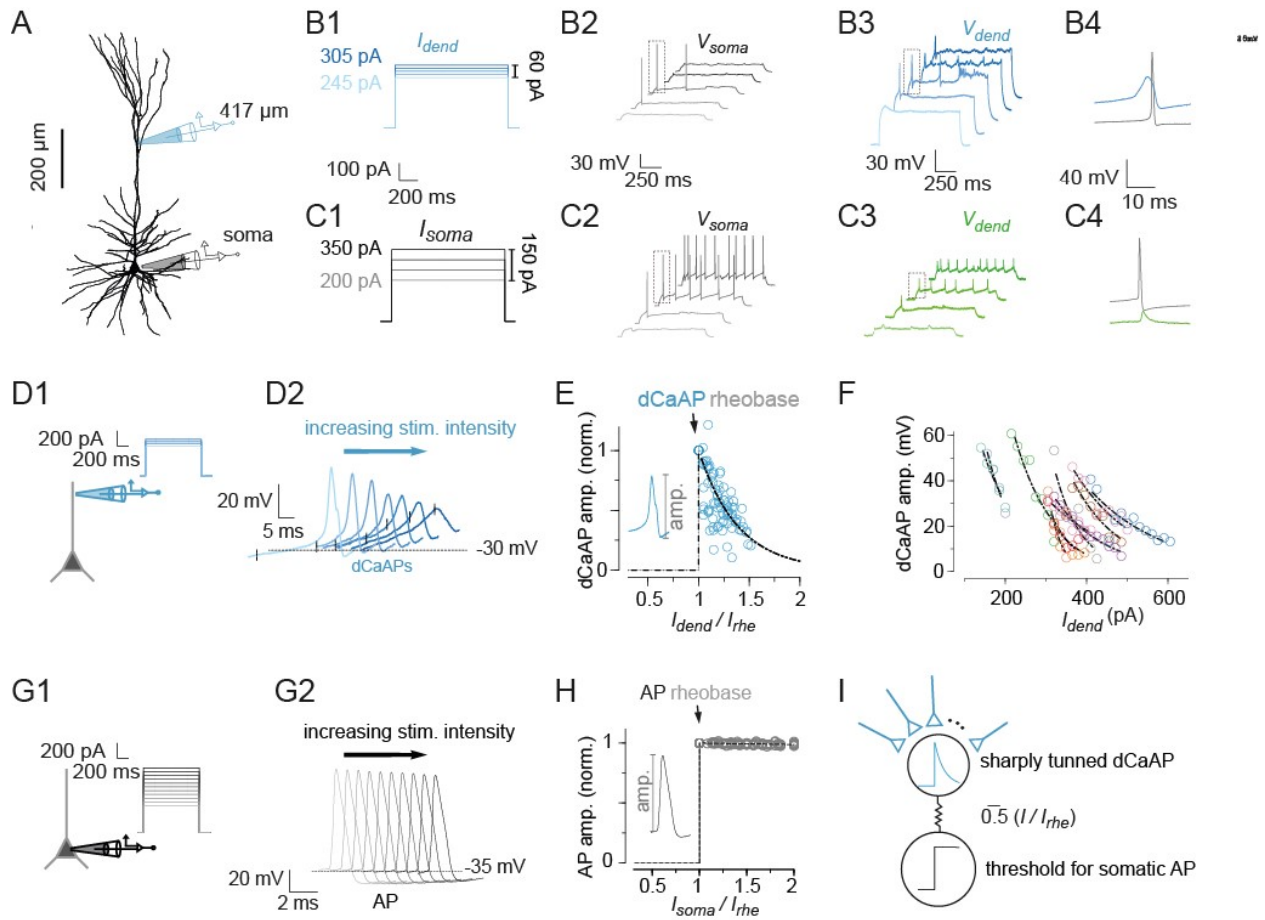
Fig. 2. Dendritic action potentials (dCaAPs) are sharply tuned to the stimulus intensity.

A. L2/3 pyramidal neuron with soma 886 μm below the pia. The somatic and dendritic electrodes are in black and blue, respectively. Recordings from this cell are shown in panels B and C. **B**. Dendritic current (I_{dend}) injected 417 μm from the soma (B1) and corresponding somatic (B2) and dendritic traces (B3). **B2.** I_{dend} of 260 pA and 275 pA, but neither smaller nor larger current, resulted in somatic APs. **B3**. dCaAP amplitudes were maximal for I_{dend} of 260 pA and 275 pA whereas $I_{dend} > 275$ pA dampened them. **B4.** dCaAP (in blue) precedes the somatic AP (in gray); traces are magnified from the framed APs in B2 and B3. **C.** Somatic current injection, I_{soma} (C1), somatic AP trains (C2) and bAP (C3) for similar ranges of current intensity as in B1. **C4.** Somatic AP (in gray) precedes the dendritic bAP (in green); traces are magnified from the framed APs in C2 and C3. **D**. Increase in I_{dend} (D1) dampened the dCaAPs' amplitude (D2); vertical tick on each trace marks 50 ms after I_{dend} onset. **E**. Amplitude of the first dCaAP in each trace against I_{dend} normalized by rheobase (I_{rhe}) for uncoupled dCaAPs (12 dendrites) and exponential fit (dashed line) with decay constant (τ_{dCaAP}) of 0.39 (median 0.38) in units of rheobase. **F**. dCaAP amplitudes as in E but not normalized by I_{rhe}. Dots in different colors represent dCaAP amplitudes from different cell (12 dendrites) with exponential fit (dashed lines). **G.** As in D but for somatic APs. I_{soma}, (G1) and the resulting somatic APs (G2). **H.** AP amplitude plotted against the normalized somatic input current strength (I_{soma}/I_{rhe}). The amplitude of the somatic AP was fixed and did not depend on I_{soma} for a range of stimuli strengths as in G2 (exponential fit with $\tau_{AP} = 82$, units of somatic I_{rhe}). **I.** Dendritic and somatic activation functions for dCaAPs (blue curve) and for somatic APs (black curve), respectively.
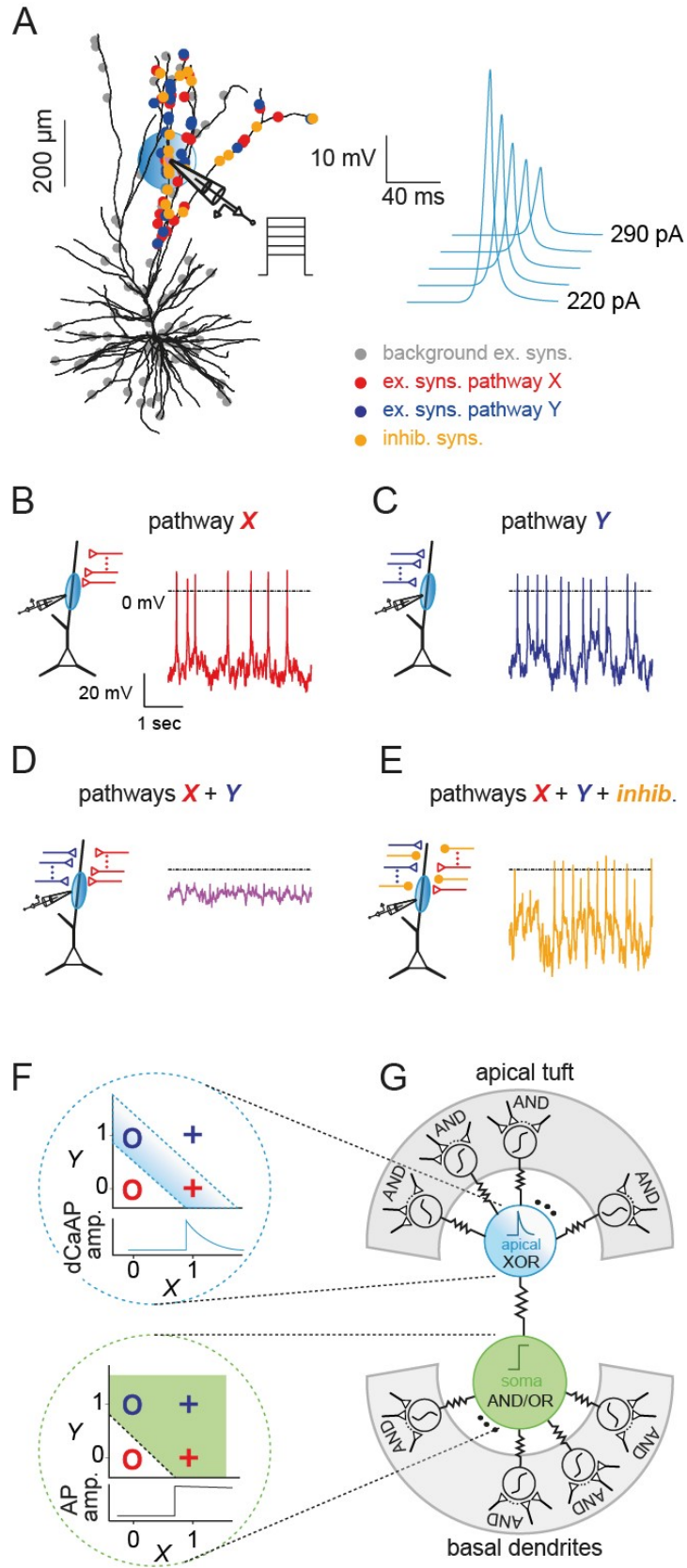
Fig. 3. Anti-coincidence in layer 2/3 of the human cortex.

A. *Left*, L2/3 neuron modeled with passive membrane and dCaAP mechanism at the apical dendrite demarcated by the blue circle (550 μm from the soma). 100 background excitatory synapses (AMPA) indicated by gray dots were randomly distributed over the entire dendritic tree and were activated in simulations B – E. Pathway *X* and *Y* with 25 excitatory synapses each (red and blue dots) modelled by AMPA and NMDA conductances (*33*) targeted a subregion of the apical dendrite in addition to 20 GABAergic inhibitory synapses (yellow dots). For model details see **Methods**. *Right*, the modeled dCaAP amplitude depended on the stimulation current intensity (I_{dend}) with decay constant (τ_{dCaAP}) of 0.3. The dCaAP threshold was set to –36 mV with 220 pA current step. **B–C**. dCaAP at the dendrite during activity of either pathway *X* (**B**), or pathway *Y* (**C**). **D–E.** dCaAPs diminished when both, pathway *X* and *Y* were active together (**D**) but recovered with the addition of inhibition (**E**). **F.** *Top*, Solution for XOR classification problem using the activation function of dCaAP (above the abscissa). *X* and *Y* inputs to the apical dendrites triggered dCaAPs with high amplitude for (*X*,*Y*) input pairs of (1,0) and (0,1) marked by blue dash and red cross, but not for (0,0) and (1,1) marked by red dash and blue cross. *Bottom*, Solution for OR classification. Somatic AP was triggered for (*X*,*Y*) input pairs of (1,1), (0,1) and (1,0) but not for (0,0). **G.** A schematic model of a L2/3 pyramidal neuron with somatic compartment (green) presented as logical AND/OR gate with activation function of somatic AP, apical dendrite compartment as logical XOR gate and basal and tuft dendritic braches, in gray background, as logical gate AND due to the NMDA spikes (*33*).

References and Notes:

1. J. DeFelipe, L. Alonso-Nanclares, J. I. Arellano, Microstructure of the neocortex: Comparative aspects. *J. Neurocytol.* **31**, 299–316 (2002).

2. H. Mohan, M. B. Verhoog, K. K. Doreswamy, G. Eyal, R. Aardse, B. N. Lodder, N. A. Goriounova, B. Asamoah, B. Brakspear, A. B. Clementine, C. Groot, S. van der Sluis, G. Testa-Silva, J. Obermayer, Z. S. R. M. Boudewijns, R. T. Narayanan, J. C. Baayen, I. Segev, H. D. Mansvelder, D. Kock, C. P.j, Dendritic and Axonal Architecture of Individual Pyramidal Neurons across Layers of Adult Human Neocortex. *Cereb. Cortex*. **25**, 4839–4853 (2015).

3. Y. Deitcher, G. Eyal, L. Kanari, M. B. Verhoog, A. Kahou, G. Antoine, H. D. Mansvelder, D. Kock, C. P. J, I. Segev, Comprehensive Morpho-Electrotonic Analysis Shows 2 Distinct Classes of L2 and L3 Pyramidal Neurons in Human Temporal Cortex. *Cereb. Cortex*. **27**, 5398–5414 (2017).

4. J. Waters, M. Larkum, B. Sakmann, F. Helmchen, Supralinear Ca2+ Influx into Dendritic Tufts of Layer 2/3 Neocortical Pyramidal Neurons In Vitro and In Vivo. *J. Neurosci.* **23**, 8558–8567 (2003).

5. M. E. Larkum, J. Waters, B. Sakmann, F. Helmchen, Dendritic Spikes in Apical Dendrites of Neocortical Layer 2/3 Pyramidal Neurons. *J Neurosci*. **27**, 8999–9008 (2007).

6. L. Beaulieu-Laroche, E. H. S. Toloza, M.-S. van der Goes, M. Lafourcade, D. Barnagian, Z. M. Williams, E. N. Eskandar, M. P. Frosch, S. S. Cash, M. T. Harnett, Enhanced Dendritic Compartmentalization in Human Cortical Neurons. *Cell*. **175**, 643-651.e14 (2018).

7. S. L. Smith, I. T. Smith, T. Branco, M. Häusser, Dendritic spikes enhance stimulus selectivity in cortical neurons in vivo. *Nature*. **503**, 115–120 (2013).

8. J. J. Moore, P. M. Ravassard, D. Ho, L. Acharya, A. L. Kees, C. Vuong, M. R. Mehta, Dynamics of cortical dendritic membrane potential and spikes in freely behaving rats. *Science*. **355**, eaaj1497 (2017).

9. B. Sivyer, S. R. Williams, Direction selectivity is computed by active dendritic integration in retinal ganglion cells. *Nat. Neurosci.* **16**, 1848–1856 (2013).

10. S. Crochet, P. Fuentealba, I. Timofeev, M. Steriade, Selective Amplification of Neocortical Neuronal Output by Fast Prepotentials InVivo. *Cereb. Cortex*. **14**, 1110–1121 (2004).

11. Y. Kim, C.-L. Hsu, M. S. Cembrowski, B. D. Mensh, N. Spruston, Dendritic sodium spikes are required for long-term potentiation at distal synapses on hippocampal pyramidal neurons. *eLife*. **4**, e06414 (2015).

12. M. E. Larkum, J. J. Zhu, B. Sakmann, Dendritic mechanisms underlying the coupling of the dendritic with the axonal action potential initiation zone of adult rat layer 5 pyramidal neurons. *J. Physiol.* **533**, 447–466 (2001).

13. N. L. Golding, N. Spruston, Dendritic Sodium Spikes Are Variable Triggers of Axonal Action Potentials in Hippocampal CA1 Pyramidal Neurons. *Neuron*. **21**, 1189–1200 (1998).

14. L. M. Palmer, A. S. Shai, J. E. Reeve, H. L. Anderson, O. Paulsen, M. E. Larkum, NMDA spikes enhance action potential generation during sensory input. *Nat. Neurosci.* **17**, 383–390 (2014).

15. M. E. Larkum, J. J. Zhu, B. Sakmann, A new cellular mechanism for coupling inputs arriving at different cortical layers. *Nature*. **398**, 338–41 (1999).

16. N. L. Golding, H. Jung, T. Mickus, N. Spruston, Dendritic Calcium Spike Initiation and Repolarization Are Controlled by Distinct Potassium Channel Subtypes in CA1 Pyramidal Neurons. *J. Neurosci.* **19**, 8789–8798 (1999).

17. C. Labarrera, Y. Deitcher, A. Dudai, B. Weiner, A. Kaduri Amichai, N. Zylbermann, M. London, Adrenergic Modulation Regulates the Dendritic Excitability of Layer 5 Pyramidal Neurons In Vivo. *Cell Rep.* **23**, 1034–1044 (2018).

18. J. Schiller, G. Major, H. J. Koester, Y. Schiller, NMDA spikes in basal dendrites of cortical pyramidal neurons. *Nature*. **404**, 285–9 (2000).

19. M. E. Larkum, K. M. M. Kaiser, B. Sakmann, Calcium Electrogenesis in Distal Apical Dendrites of Layer 5 Pyramidal Cells at a Critical Frequency of Back-Propagating Action Potentials. *Proc. Natl. Acad. Sci.* **96**, 14600–14604 (1999).

20. M. E. Larkum, T. Nevian, M. Sandler, A. Polsky, J. Schiller, Synaptic integration in tuft dendrites of layer 5 pyramidal neurons: a new unifying principle. *Science*. **325**, 756–760 (2009).

21. J. J. Zhu, Maturation of layer 5 neocortical pyramidal neurons: amplifying salient layer 1 and layer 4 inputs by Ca2+ action potentials in adult rat tuft dendrites. *J. Physiol.* **526**, 571–587 (2000).

22. J. Schiller, Y. Schiller, G. Stuart, B. Sakmann, Calcium action potentials restricted to distal apical dendrites of rat neocortical pyramidal neurons. *J Physiol*. **505 (Pt 3)**, 605–16 (1997).

23. M. L. Hines, N. T. Carnevale, The NEURON simulation environment. *Neural Comput.* **9**, 1179–1209 (1997).

24. M. London, M. Häusser, Dendritic computation. *Annu Rev Neurosci*. **28**, 503–532 (2005).

25. A. Polsky, B. W. Mel, J. Schiller, Computational subunits in thin dendrites of pyramidal cells. *Nat Neurosci*. **7**, 621–627 (2004).

26. A. Losonczy, J. C. Magee, Integrative Properties of Radial Oblique Dendrites in Hippocampal CA1 Pyramidal Neurons. *Neuron*. **50**, 291–307 (2006).

27. E. Boldog, T. E. Bakken, R. D. Hodge, M. Novotny, B. D. Aevermann, J. Baka, S. Bordé, J. L. Close, F. Diez-Fuertes, S.-L. Ding, N. Faragó, Á. K. Kocsis, B. Kovács, Z. Maltzer, J. M. McCorrison, J. A. Miller, G. Molnár, G. Oláh, A. Ozsvár, M. Rózsa, S. I. Shehata, K. A. Smith, S. M. Sunkin, D. N. Tran, P. Venepally, A. Wall, L. G. Puskás, P. Barzó, F. J. Steemers, N. J. Schork, R. H. Scheuermann, R. S. Lasken, E. S. Lein, G. Tamás, Transcriptomic and morphophysiological evidence for a specialized human cortical GABAergic cell type. *Nat. Neurosci.* **21**, 1185 (2018).

28. A. Gidon, I. Segev, Principles Governing the Operation of Synaptic Inhibition in Dendrites. *Neuron*. **75**, 330–341 (2012).

29. A. T. Gulledge, G. J. Stuart, Excitatory Actions of GABA in the Cortex. *Neuron*. **37**, 299–309 (2003).

30. G. M. Shepherd, R. K. Brayton, Logic operations are properties of computer-simulated interactions between excitable dendritic spines. *Neuroscience*. **21**, 151–165 (1987).

31. M. L. Minsky, *Perceptrons: An Introduction to Computational Geometry* (MIT Press, Cambridge/Mass., 1969).

32. F. Rosenblatt, *The perceptron, a perceiving and recognizing automaton Project Para* (Cornell Aeronautical Laboratory, 1957).

33. G. Eyal, M. B. Verhoog, G. Testa-Silva, Y. Deitcher, R. Benavides-Piccione, J. DeFelipe, D. Kock, C. P. J, H. D. Mansvelder, I. Segev, Human Cortical Pyramidal Neurons: From Spines to Spikes via Models. *Front. Cell. Neurosci.* **12** (2018), doi:10.3389/fncel.2018.00181.

34. P. Poirazi, T. Brannon, B. W. Mel, Pyramidal Neuron as Two-Layer Neural Network. *Neuron*. **37**, 989–999 (2003).

35. G. Testa-Silva, S. Honnuraiah, C. French, J. King, K. Drummond, L. M. Palmer, G. J. Stuart, NMDA spikes in human neocortex. *Program No 46312 2018 Neurosci. Meet. Plan. San Diego CA Soc. Neurosci. 2018 Online* (2018).

36. G. Testa-Silva, M. B. Verhoog, N. A. Goriounova, A. Loebel, J. J. J. Hjorth, J. C. Baayen, C. P. J. de Kock, H. D. Mansvelder, Human Synapses Show a Wide Temporal Window for Spike-Timing-Dependent Plasticity. *Front. Synaptic Neurosci.* **2** (2010), doi:10.3389/fnsyn.2010.00012.

37. J. T. Ting, T. L. Daigle, Q. Chen, G. Feng, Acute brain slice methods for adult and aging animals: application of targeted patch clampanalysis and optogenetics. *Methods Mol. Biol. Clifton NJ*. **1183**, 221–242 (2014).

38. T. Nevian, M. E. Larkum, A. Polsky, J. Schiller, Properties of basal dendrites of layer 5 pyramidal neurons: a direct patch-clamp recording study. *Nat. Neurosci.* **10**, 206–214 (2007).

39. S. A. Booker, J. Song, I. Vida, Whole-cell patch-clamp recordings from morphologically- and neurochemically-identified hippocampal interneurons. *J. Vis. Exp. JoVE*, e51706 (2014).

40. M. H. Longair, D. A. Baker, J. D. Armstrong, Simple Neurite Tracer: open source software for reconstruction, visualization and analysis of neuronal processes. *Bioinforma. Oxf. Engl.* **27**, 2453–2454 (2011).

41. L. Feng, T. Zhao, J. Kim, neuTube 1.0: A New Design for Efficient Neuron Reconstruction Software Based on the SWC Format. *eNeuro*. **2** (2015), doi:10.1523/ENEURO.0049-14.2014.

42. G. Eyal, M. B. Verhoog, G. Testa-Silva, Y. Deitcher, J. C. Lodder, R. Benavides-Piccione, J. Morales, J. DeFelipe, C. P. de Kock, H. D. Mansvelder, I. Segev, Unique membrane properties and enhanced signal processing in human neocortical neurons. *eLife*. **5** (2016), doi:10.7554/eLife.16553.

43. R. D. Traub, R. K. Wong, R. Miles, H. Michelson, A model of a CA3 hippocampal pyramidal neuron incorporating voltage-clamp data on intrinsic conductances. *J Neurophysiol*. **66**, 635–50 (1991).

44. L. Sarid, R. Bruno, B. Sakmann, I. Segev, D. Feldmeyer, Modeling a layer 4-to-layer 2/3 module of a single column in rat neocortex: interweaving in vitro and in vivo experimental observations. *Proc. Natl. Acad. Sci. U. S. A.* **104**, 16353–16358 (2007).

45. P. Rhodes, The properties and implications of NMDA spikes in neocortical pyramidal cells. *J Neurosci*. **26**, 6704–15 (2006).

46. A. Gupta, Y. Wang, H. Markram, Organizing principles for a diversity of GABAergic interneurons and synapses in the neocortex. *Science*. **287**, 273–278 (2000).

47. I. Reuveni, A. Friedman, Y. Amitai, M. J. Gutnick, Stepwise repolarization from Ca2+ plateaus in neocortical pyramidal cells: evidence for nonhomogeneous distribution of HVA Ca2+ channels in dendrites. *J. Neurosci.* **13**, 4609–4621 (1993).

48. Z. M. Khaliq, N. W. Gouwens, I. M. Raman, The Contribution of Resurgent Sodium Current to High-Frequency Firing in Purkinje Neurons: An Experimental and Modeling Study. *J. Neurosci.* **23**, 4899–4912 (2003).

49. R. Latorre, K. Castillo, W. Carrasquel-Ursulaez, R. V. Sepulveda, F. Gonzalez-Nilo, C. Gonzalez, O. Alvarez, Molecular Determinants of BK Channel Functional Diversity and Functioning. *Physiol. Rev.* **97**, 39–87 (2016).

50. A. Destexhe, A. Babloyantz, T. J. Sejnowski, Ionic mechanisms for intrinsic slow oscillations in thalamic relay neurons. *Biophys. J.* **65**, 1538–1552 (1993).

NEURON simulation files are available in http://modeldb.yale.edu/254217 for Fig. 3 and S9 and for http://modeldb.yale.edu/260178 Fig. S12 (password: gidon2019). These models will be publically available after publication).

Reconstructed neurons and graphs with corresponding data are stored at https://zenodo.org/.

5

Supplementary Materials for

Dendritic action potentials and computation in human layer 2/3 cortical neurons

Albert Gidon, Timothy Adam Zolnik, Pawel Fidzinski, Felix Bolduan, Athanasia Papoutsi, Panayiota Poirazi, Martin Holtkamp, Imre Vida, Matthew Evan Larkum*

*Corresponding author E-mail: matthew.larkum@hu-berlin.de

This PDF file includes:
Materials and Methods
Figs. S1 to S12
Tables S1 and S2 (*36-50*)

Materials and Methods

Human tissue transport and preparation

All human experiments were approved by the Ethics Committee of the Charité – Universitätsmedizin Berlin and performed in agreement with the Declaration of Helsinki. Neocortical tissue used in this study was obtained from resections of the anterior temporal lobe of twenty-seven epilepsy patients and of three brain tumor patients (**Table S1**). All patients had given written consent prior to the procedure. The brain tissue used in this study was presumably non-pathological, as it was not located in the area of the seizure focus or the tumor. Immediately after removal, tissue was transferred to carbonated (95% O_2, 5% CO_2), ice-cold transport protective solution; either "NMDG" [containing (in mM) NMDG (93), HCl (93), KCl (2.5), NaH_2PO_4 (1.2), $NaHCO_3$ (30), $MgSO_4$ (10), $CaCl_2$ 141 (0.5), HEPES (20), glucose (25), Na-L-ascorbate (5), thiourea (2), Na-pyruvate (3) (ref *3*)] or in "Choline" solution [containing (in mM) Choline chloride (110), KCl (2.5), NaH_2PO_4 143 (1.25), $NaHCO_3$ (26), $MgCl_2$ (7), $CaCl_2$ (0.5), glucose (10), Na-L-ascorbate (11.6), Na-144 pyruvate (3.1) (ref *36*)] and transported within 10-40 minutes to the location where pia was carefully removed and then transported a second time, within 5 minutes in the same ice-cold transport solution, to the laboratory for slicing and recording. Tissue resected from tumor patients was transported and sliced in "Sucrose" solution [containing (in mM) NaCl (87), NaH_2PO_4 (1.25), KCl (2.5), $CaCl_2$ (0.5), $MgCl_2$ (3) Glucose (10), $NaHCO_3$ (25), Saccharose (75)]. Cortical tissue was sliced to thickness of 300-350 μm with Leica 1200vt vibrotome in protective Choline solution with the blade oriented as orthogonally to the pia as possible to maintain complete dendrites. Slices were incubated in either "HEPES"

solution [identical to NMDG solution but with NaCl (92) instead of NMDG (93) and HCl (93) (ref *37*)] or "aCSF" [containing (in mM) NaCl (125), KCl (2.5), NaH2PO4 (1.25), NaHCO3 (25), MgCl2 (1), CaCl2 141 (1), glucose (25)] solution in 35° C for at least 30 minutes and then stored in aCSF continuously perfused with carbogen for the rest of the experiment in room temperature no longer than 24 hours.

Electrophysiology

Slices were submerged in the recording chamber and perfused with aCSF (~2 ml/min) and heated to 33-35°C (Scientifica). Single L2/3 pyramidal neurons were identified using infrared Dodt gradient contrast and a CCD camera (CoolSnap ES2; Roper Scientific). Data were acquired with InstruTECH ITC-18 board and custom software written in Igor (Igor 7; Wavemetrics). The direct (point-to-point) distance of the soma from pia and the distance of the dendritic electrode from the soma were measured during the recording session. Cells were chosen randomly. Recording pipettes were filled with intracellular solution containing 0.1% Biocytin and (in mM), K-gluconate (130), KCl (20), Mg-ATP (4), Na_2-phosphocreatine (10), GTP-Tris (0.3), HEPES (10). The pH was adjusted with KOH to $7.25 - 7.30$. Osmolality was 300 mosmol l^{-1}. In addition, the somatic pipette contained $10 - 20$ μM Alexa 594 (Invitrogen).

Dual whole-cell voltage recordings were performed from the soma and dendrites using Dagan BVC-700A amplifiers (Dagan Minneapolis, USA) with low pass filter set to 5 KHz. We did not correct for liquid junction potential. Pipette resistance and access resistance were typically $4 - 12$ MΩ and $12 - 20$ MΩ for the somatic pipette. Due to the small diameter (*3*) of the dendrites of L2/3 neurons, the dendritic pipette resistance and access resistance was $14 - 32$ MΩ and $40 - 200$ MΩ respectively (*38*).

Access resistance and capacitance were continuously monitored for the dendritic electrode in current clamp mode. For the voltage attenuation plot in **Fig. S1**D, in addition to the manual compensation of the dendritic pipette access resistance during the experiment, we further corrected access resistance offline by fitting single exponential curve to the last 4 ms of the voltage response to the current test pulse (test pulse had duration of 5 ms and amplitude of –60 nA). Then, the exponential fit was extrapolated to the beginning of the stimulus time to get the expected voltage. The difference between the experimentally measured voltage and the voltage computed by the exponential fit was used to find the additional access resistance which was insufficiently compensated during the experiment.

Statistical analysis

Wilcoxon rank-sum test for two independent samples was used using Igor (WaveMetrix) built-in operation.

Visualization of biocytin-filled neurons

To morphologically identify and characterize recorded neurons, the acute human slices were processed for histology as previously described (*39*). In brief, slices were fixed at least for 24 hours in phosphate buffered (PB) solution (0.1 M) containing 4% paraformaldehyde. Subsequently, slices were intensely rinsed and incubated with Alexa Flour 647-conjugated streptavidin (Invitrogen, UK, dilution 1:1000 in PB, including 0.1% Triton-X100 as detergent) overnight at 4°C. Slices were finally mounted in an aqueous mounting medium (Fluoromount,

Southern Biotech, AL, USA) either on glass slides with a cover slip or between two coverslips with a 300 µm metal spacer.

Confocal imaging and reconstruction of neurons

Cells were imaged on a laser scanning confocal microscope (FluoView 1000, Olympus) using a 20x (N.A 0.75) or a 30x (N.A 1.05) silicon oil-immersion objective. Image stacks were collected at 1024x1024 resolution in the horizontal plan (2µs pixel dwell time) and 1 µm steps along the Z-axis. Image stacks covering the full extent of the neuron were stitched using the FIJI software package(40) (http://fiji.org) and 3D reconstructions of the somato-dendritic domain of selected cells were performed using the neuTube software package (41).

Two–photon imaging.

Cells were filled with 100 µM Oregon-green 488 BAPTA-1 (Thermo Fischer, Wlatham, MA) by dialysis from the patch pipette in whole-cell configuration. Cells were stimulated 10x with 2 ms current steps at 50 Hz and 200 Hz. Line scan recordings began typically 40 minutes (~ 30–120 min) after break-in and were performed chronologically from soma to dendrite. Data acquisition was performed using MATLAB (MathWorks Inc.) based MES software package (Femtonics). Calcium signals were imaged with a Femto 2D two-photon laser scanning system (Femtonics Ltd, Budapest, Hungary) equipped with a femtosecond pulsed Chameleon Ti:Sapphire laser (Coherent, Santa Clara, CA, USA) tuned to $\lambda = 800$ nm. Fluorescence was detected in epifluorescence mode with a water immersion objective (LUMPLFL ×60/1.0 NA, Olympus,

Hamburg, Germany) and 525/50 bandpass filter. Trans-fluorescence and transmitted infrared light were detected using an oil immersion condenser (Olympus; 1.4 NA).

Fluorescence resulted from Ca^{2+} transients were acquired with 64-pixel line scans with an average 0.5 kHz sampling rate (minimum 48 Hz and maximum of 1.5 kHz). Individual traces were oversampled offline (interpolation) to 1.5 kHz (i.e. maximum sample rate) and averaged over at least 4 repetitions and smoothed by 5 points boxcar filter. Ca^{2+} transients are reported here as the peak change in OGB-1 fluorescence ($F(t)$) normalized to the resting OGB fluorescence (F_0) after subtracting the background fluorescence from neighboring regions F_{bg},

$$\Delta F/F_0 = (F(t) - F_0)/(F_0 - F_{bg}). \tag{1}$$

The fluorescence against the distance from the soma were fitted by a skewed Gaussian curve using the equation $y = a(x - c)^b \times exp((x - c)^2/d^2)$ where a, b, c, and d are fitting parameters.

Computational model

We used a reconstruction of L2/3 neuron morphology (**Fig. 3A**), consisting of a somatic compartment, 101 basal dendritic sections, 81 apical tree sections and an axonal cable (1000 μm length, 1μm diameter). For each section compartment lengths were at most 30 μm. Membrane capacitance (C_m) and axial resistance (R_i) were uniformly set to 0.45 μF cm^2 (42) and 100 Ω×cm, respectively, over the entire dendrite. These values resulted in somatic input resistance (R_{in}) and membrane time constant (τ_m) of 39 MΩ and 17 ms, respectively, similar to the experimental values (R_{in} = 41 MΩ and τ_m = 14 ms). The soma was modeled with sodium (I_{Na}), potassium delayed rectifier (I_{Kdr}) currents, with the corresponding maximal conductances, g_{Na} = 0.1 S/cm^2 ,

g_K = 0.045 S/cm^2 and reversal potentials, E_K = –80 mV, E_{Na} = 90 mV. R_m was 37 MΩ×cm^2 in all compartments. The rate functions for the sodium and potassium channels where taken from (*43*), but all activation curves were shifted by –50 mV (originally –60 mV in (*43*)) to account for somatic threshold we observed in the experiment (complete model for **Fig. 3** and **Fig. S9** is publically available in ModelDB)

dCaAPs were simulated at one dendritic compartment where threshold, width and amplitude as a function of the input strength were simulated by sum of current sources with a sigmoidal shape. Specifically, the dCaAP current,

$$I_{dCaAP} = -wK(v)(A - B),$$ (2)

was triggered when membrane potential crossed –36 mV where w was 1.6 and 4 such that the dCaAP amplitude was about 50 mV and 60 mV at threshold in **Fig. 3** and in **Fig. S9**, respectively.

A and B, the rise and decay of the dCaAP current were given by sigmoid functions $A = 1/(1 + exp(-(t - t')/\tau_A))$ and $B = 1/(1 + exp(-(t - (t' + \Delta t')/\tau_B))$ where t' is the dCaAP onset, $\Delta t'$ = 21 ms, τ_A = 3 ms and τ_B = 0.4 ms. The dendrite activation function, $K(v)$, which depended on membrane potential, (where in our passive dendritic model approximate dCaAP suppression as a function of the current $K(i)$), was

$$K(v) = exp[\frac{-F \times (v - v_{th})}{\tau_K}]$$ (3)

where v is the membrane potential at the location of the dCaAP, v_{th} is the threshold (–36 mV) for dCaAP, $F = 1/(v_{th} - v_{rest})$, is a normalization factor and τ_K, the dCaAP amplitude decay constant was 0.3 (dimensionless). The refractory period was explicitly set to 200 ms such that dCaAPs fired with 5 Hz or less. Synaptic model was done similarly to refs (*33, 44, 45*).

All the synapses were activated at 20 Hz in all the models. The synaptic current was modeled as, $I_{syn}(t, V) = g_{syn}(t, V) \times (V - E_{syn})$, where $g_{syn}(t, V)$ is the synaptic conductance change, and E_{syn} is the reversal potential for the synaptic current which was 0 mV for excitatory synapses and –75 mV for inhibitory synapses. The conductance change for AMPA, NMDA and GABA was modeled as

$$g_{syn}(t, V) = g_{max} \times N \times G \times (e^{-t/\tau_2} - e^{-t/\tau_1}) , \tag{4}$$

where N is normalization factor such that g_{max} the peak conductance. g_{max} and time constants where as follows: $g_{max,AMPA} = 0.7$ nS, $g_{max,NMDA} = 1.3$ nS, $g_{max,GABA} = 0.5$ nS, $\tau_{1,AMPA} = 0.3$ ms, $\tau_{2,AMPA} = 1.8$ ms, $\tau_{1,NMDA} = 8$ ms, $\tau_{2,NMDA} = 35$ ms, $\tau_{1,GABA} = 2$ and $\tau_{2,GABA} = 23$ ms (**Fig. 3** and distal inhibition in **Fig. S9**), $\tau_{1,GABA\text{-}proximal} = 0.5$ and $\tau_{2,GABA\text{-}proximal} = 5$ ms (**Fig. S9**, proximal inhibition). For AMPA and GABA, we used $G = 1$, whereas for NMDA

$$G = \frac{1}{1 + e^{-\gamma v} \times [Mg^{2+}]/3.57} , \tag{5}$$

where $[Mg^{2+}]$ is extracellular magnesium concentration of 1 mM, $\gamma = 0.077$ 1/mV (*33*).
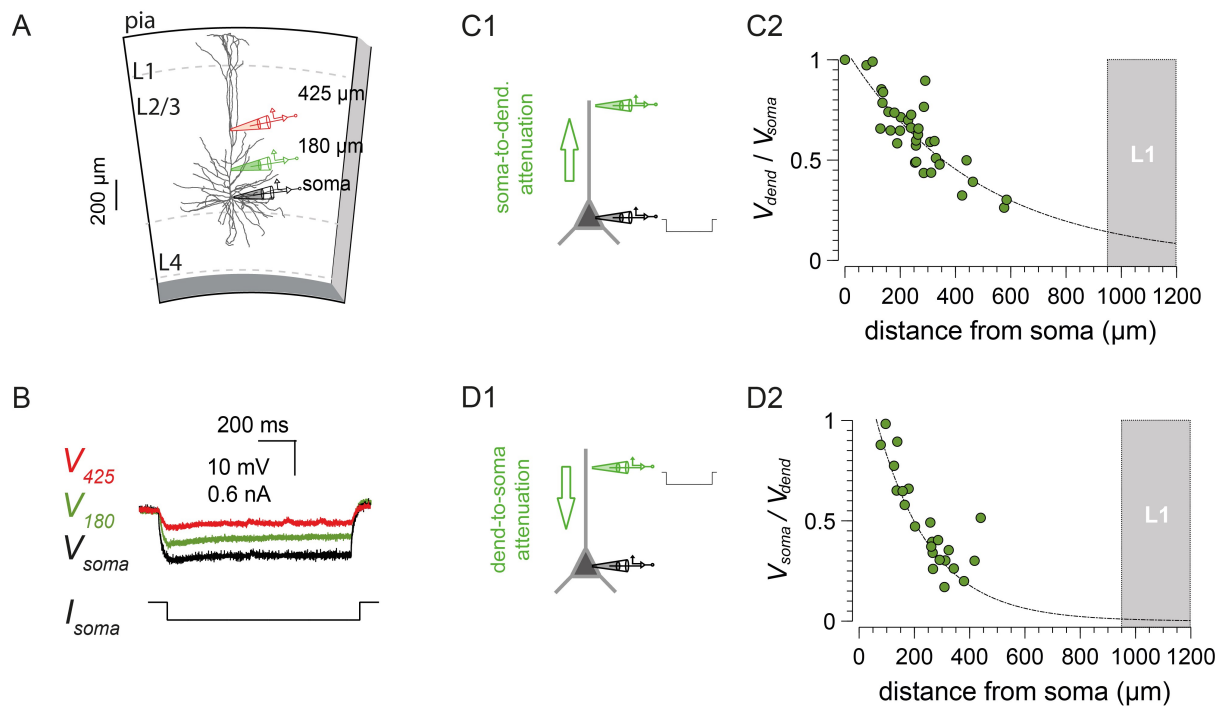
Fig. S1. Steady potentials are severely attenuated at the apical dendrite of layer 2/3 pyramidal neurons in the human cortex.

A. Reconstructed cortical layer 2/3 pyramidal neuron at a depth of 1098 μm from the pia. **B**. Two consequent dual recordings of soma and dendrites during somatic negative step current injection. The traces' color corresponds to the color of the patch clamp electrodes in **A** in the two dendritic sites. **C1**. Experimental schematic depicts stimulation (negative current step for one second) and recording site at the soma (black pipette) and a second recording site at the dendrite. **C2**. Attenuation of steady potentials (averaged for voltage traces between 800 and 1000 ms after stimulation onset; $n = 34$) from the soma to the dendrite (dendritic potential normalized by the somatic potential) plotted against the distance of the dendritic recording electrode. Length constant is $\lambda = 475$ μm (single exponential fit). Gray region on the graph depicts a putative region of layer 1 for the longest dendrites. **D1**. As in C1 but current was injected into the dendrite rather than the soma. **D2**. As in C2 but for the potential attenuation from the dendrite to the

soma. Length constant was $\lambda = 195$ μm (single exponential fit; $n = 23$; average R_{access} of 71.3 $\pm$ 19.5 MΩ ranging between 38.0 and 113.4 ms). The amplitude of the exponential fit in C2 and D2 was not constrained to value of 1 at the soma.
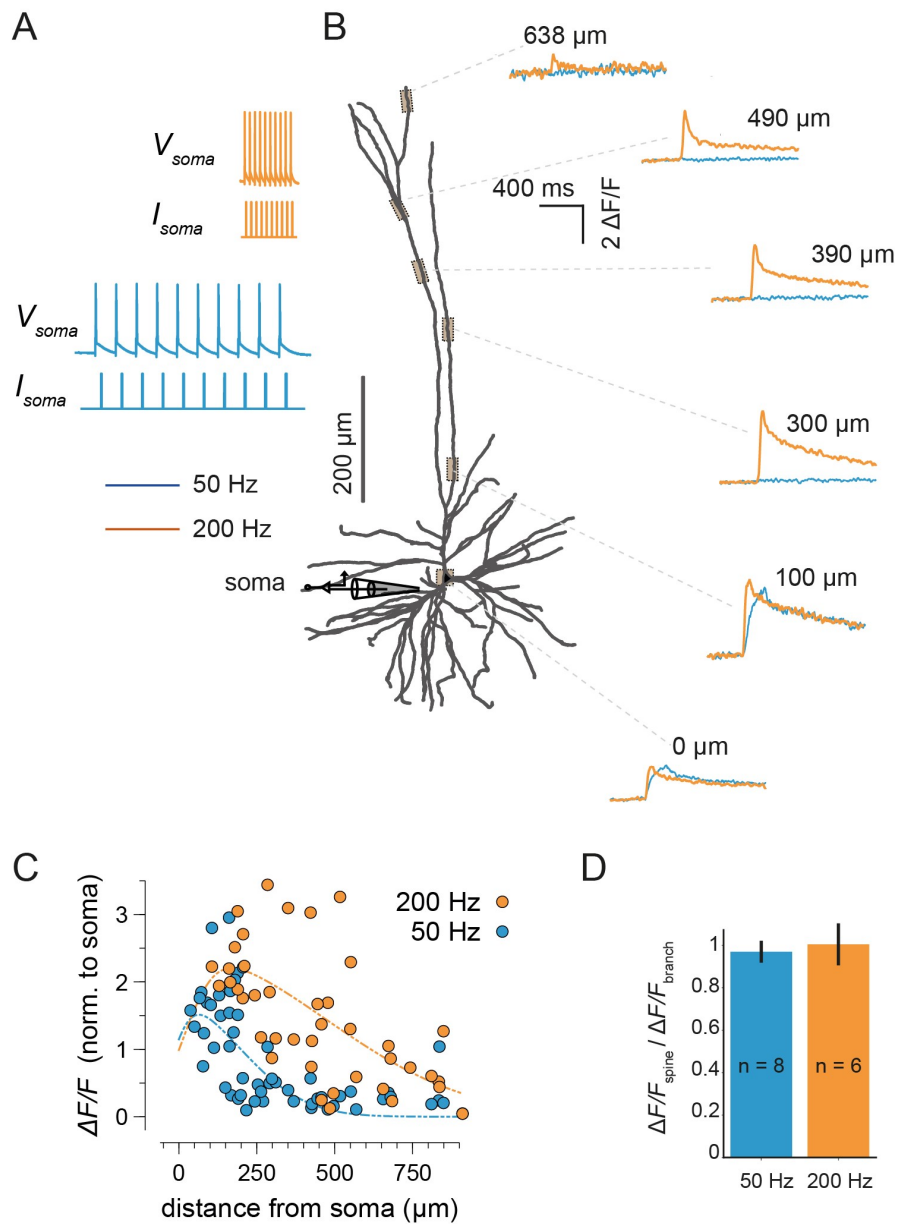
Fig. S2. 2-photon imaging indicates that APs invade the distal dendrite at high frequency.

A. AP bursts were evoked by injecting 10 supra-threshold current pulses of 2 ms duration at 50 Hz (blue traces) and at 200 Hz (orange traces) at the soma of layer 2/3 pyramidal neurons. **B.** Example of Ca^{2+} signals in a pyramidal neuron located 640 μm below the pia surface. Dendritic locations where imaged sequentially. $\Delta F/F$ traces are shown with corresponding color (blue and

orange for somatic pulses at 50 Hz and 200 Hz, respectively). **C.** Summary for amplitude of $\Delta F/F$ for somatic current pulse stimulation at 50 Hz (blue dots; $n = 18$ cells) and at 200 Hz (orange dots; $n = 13$ cells). Note the enhanced $\Delta F/F$ response for stimulation at 200 Hz (fitted with scaled skewed Gaussian (*4*)). **D.** Ca^{2+} signal at the spine ($\Delta F/F_{spine}$) was very similar to the corresponding signal at the branch ($\Delta F/F_{branch}$) for both 50 Hz and 200 Hz APs burst frequency.
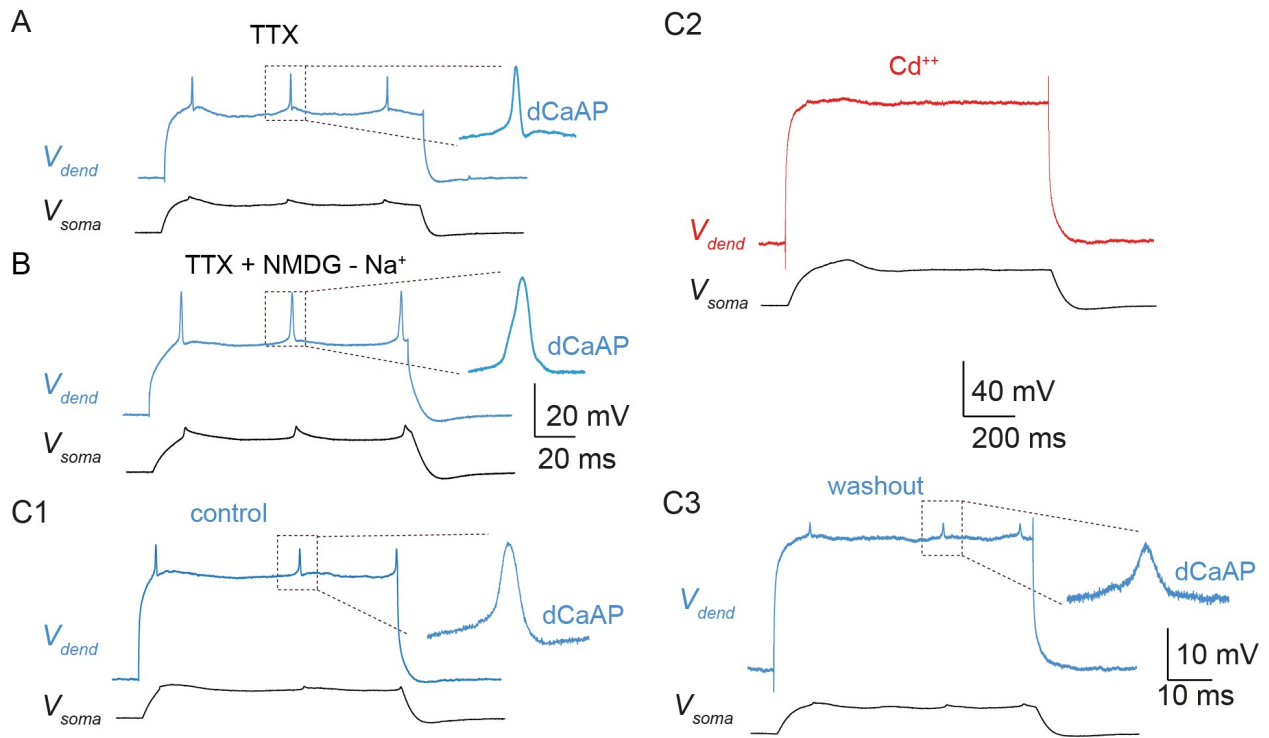
Fig. S3. Dendritic APs were blocked by the voltage gated calcium channel blocker, Cd^{2+}, and were not blocked by Na^{+} channel blocker, TTX.

In all panels dendritic voltage (top trace in blue/red) and somatic voltage (bottom trace in black) are shown in response to a current step injected by the dendritic electrode. **A.** Dendritic APs were recorded in the presence of TTX (1 μM; $n = 4$) in the recording chamber. Dendritic electrode was located 306 μm from the cell body. **B.** As in A in another cell with dendrite electrode 260 μm from the soma. In addition NMDG was used here as substitution for the sodium ions in the extracellular solution to exclude the possibility that dCaAPs are triggered by TTX-insensitive sodium channels. In A and B framed dCaAPs are magnified on the right with scale bar in B. **C.** Step current injected by the dendritic electrode (279 μm from the soma) triggered uncoupled dCaAPs (C1) blocked by Cd^{2+} ($n = 5$ cells) (C2). dCaAPs reappeared after Cd^{2+} washout (C3;

3/5 dendrites recorded for sufficient time, >20 min, to allow washout). The framed dCaAP is

magnified on the right. Scale bar for traces in A–C is shown in the bottom of C2.
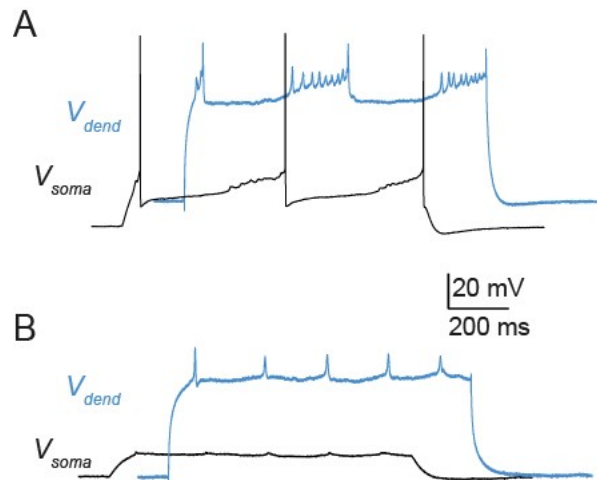
5

Fig. S4. dCaAPs in the pyramidal neurons of L2/3 in neocortical tissue obtained from tumor patients.

Dendritic voltage (top trace in blue) and somatic voltage (bottom trace in black) in response to current step injected by the dendritic electrode. Dendritic voltage traces are presented with an offset to the right with respect to the somatic traces. **A.** dCaAPs in L2/3 pyramidal neuron in the right temporo-mesial cortex resected from a tumor patient. The neuron was located at depth of 767 µm from the pia and the dendritic electrode was located 291 µm from the soma. The dendrite fired burst of complex-coupled dCaAPs. **B.** Simple-uncoupled dCaAPs recorded in a L2/3 pyramidal neuron (682 µm from the pia with the dendritic electrode at 267 µm from the soma) from the left temporo-mesial cortex resected from a different tumor patient from A.
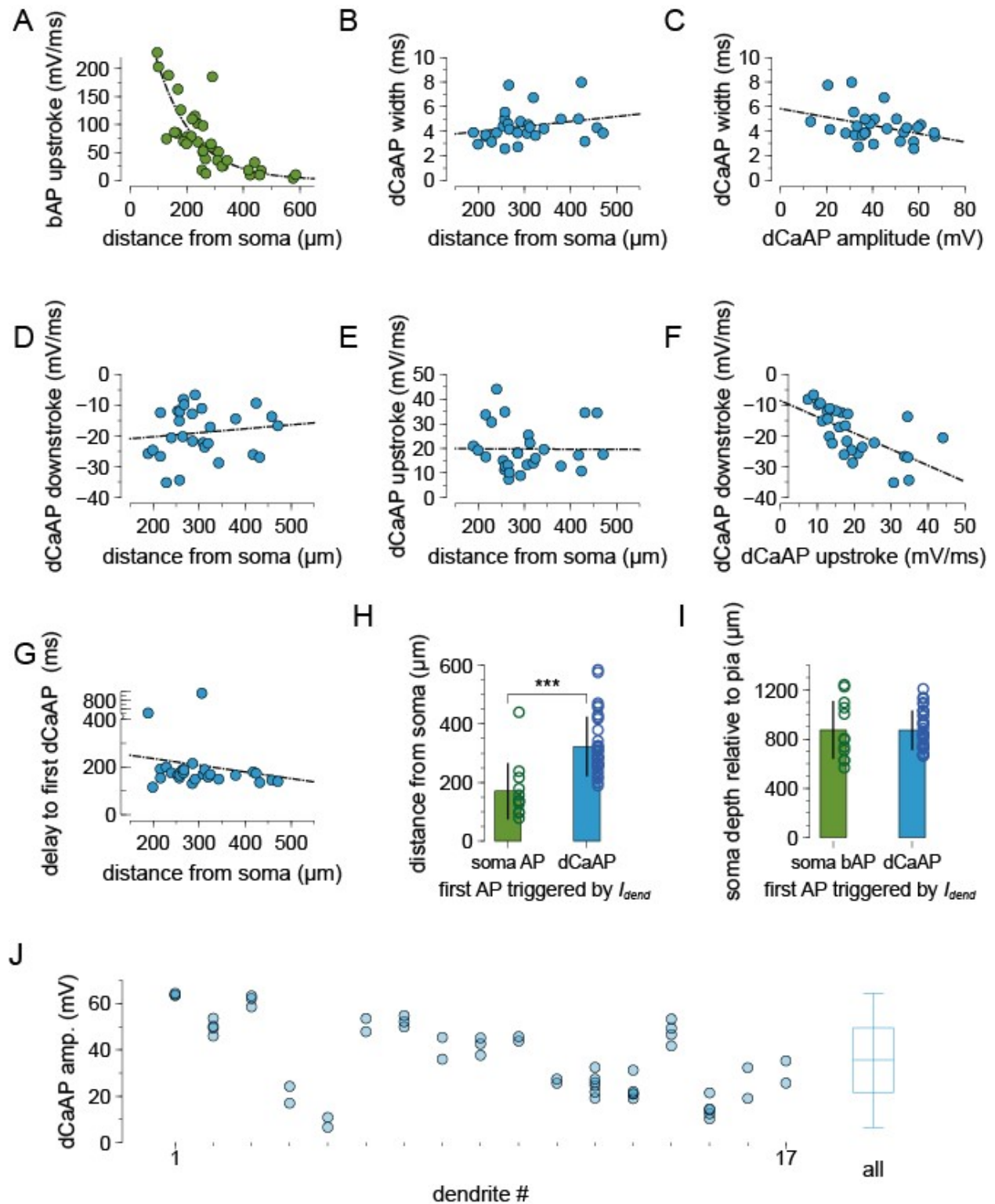
Fig. S5. Properties of bAPs and dCaAPs at threshold in human layer 2/3 neurons.

A. bAP upstroke maximal derivative against the distance of the recording electrode from the soma and exponential fit with decay constant $\lambda = 121$ μm ($n = 31$). B. dCaAP upstroke as a function of the recording distance from the soma is weakly correlated with distance ($r^2 = 0.1$; $n = 28$). **B–E.** dCaAPs' upstroke (B; $r^2 = 4.6 \times 10^{-5}$), width (C; at half of the amplitude; $r^2 = 0.058$), downstroke (D; maximal derivative; $r^2 = 0.017$) and the delay to the first AP from stimulation onset (E; $r^2 = 0.18$) are independent or weakly dependent of the distance of the recording electrode from the soma. **F.** dCaAP's widths weakly depended on the dCaAP's amplitudes ($r^2 = 0.13$). **G.** dCaAP's upstrokes and downstrokes are correlated ($r^2 = 0.4$). In B–G $n = 28$ dendrites were used. For consistency with all traces, results are shown for the first dCaAP. **H.** Dendritic electrode evoked somatic APs at proximal regions (170 ± 93 μm from the soma) and dCaAPs at the distal regions (323 ± 99 μm from the soma; Wilcoxon rank-sum test, $p < 10^{-5}$). **I.** Dendritic electrode evoked either somatic APs or dCaAPs independently of the depth of the soma from the pia (the cortical surface). **H.** dCaAP's amplitudes in single near threshold traces in 17 dendrites. Average coefficient of variation was 0.116.
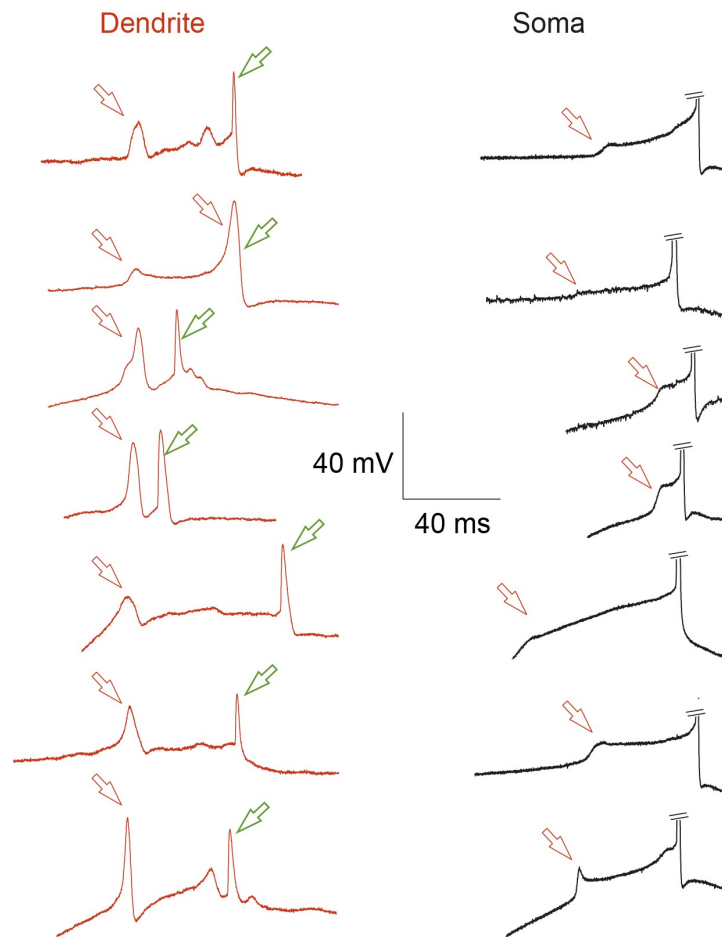
Fig. S6. Gallery of complex dCaAPs.

Left column, dCaAPs (indicated by red arrows) followed by bAPs (green arrows) in response to a

dendritic current step injection. *Right column*, Somatic APs (truncated) and dCaAPs (red arrow)

recorded at the soma. Somatic APs in these traces were only evoked when preceded by dCaAPs.
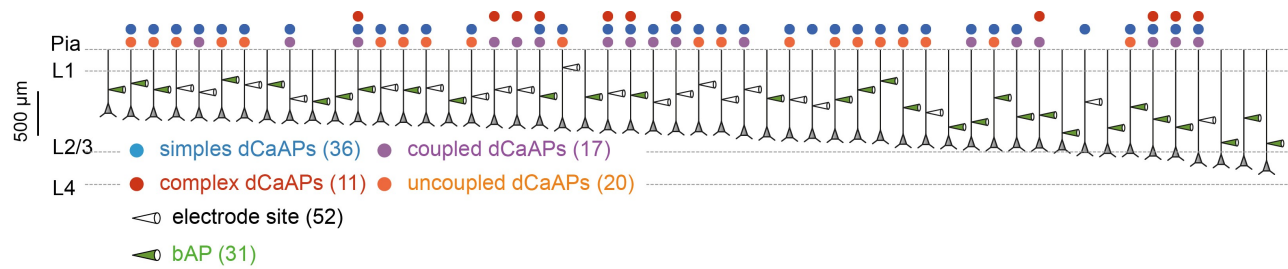
Fig. S7. Summary of bAPs and dCaAPs recordings in L2/3 in the human neocortex.

A schematic drawing summarizing the site of the dendritic electrodes and depth of the somata of the 52 dendrites recoded in this study. Green electrode marker depicts bAP recording. The color-coded dots above each neuron indicate that dCaAPs were either coupled or uncoupled with somatic AP (mutually exclusive classification) and whether dCaAPs were complex and/or simple in these dendrites. The total number of cells for each condition is shown in parentheses.
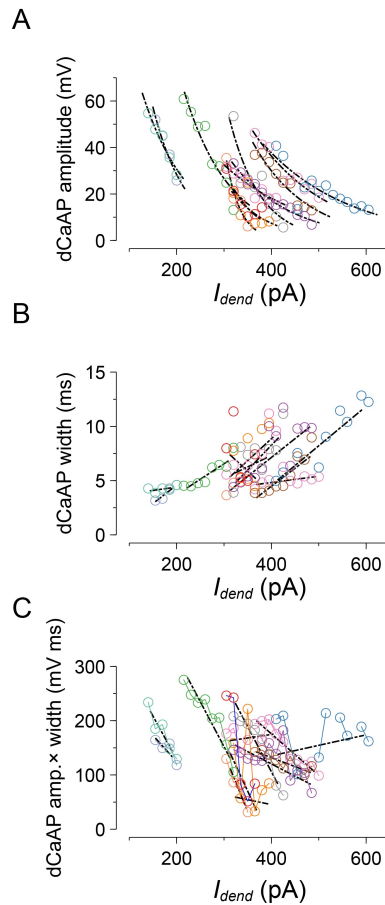
Fig. S8. dCaAPs width and amplitude as a function of the stimulus intensity.

A. (Copied from **Fig. 2E** for comparison) dCaAP amplitudes plotted against the input current strength (I_{dend}) for uncoupled dCaAPs (12 dendrites), fitted by exponential curves (dashed line). Dots in different colors represent dCaAP amplitudes from different cell (12 dendrites). **B.** dCaAP widths at half of the amplitude increases with I_{dend} for the cells in A (a linear fit for each cell is plotted in black dashed line). **C.** dCaAP amplitude × width (an approximation to the dCaAP integral) decreases with I_{dend} namely, the increase in dCaAP width did not counteract the amplitude decay effectively (a linear fit for each cell is plotted in black dashed line).
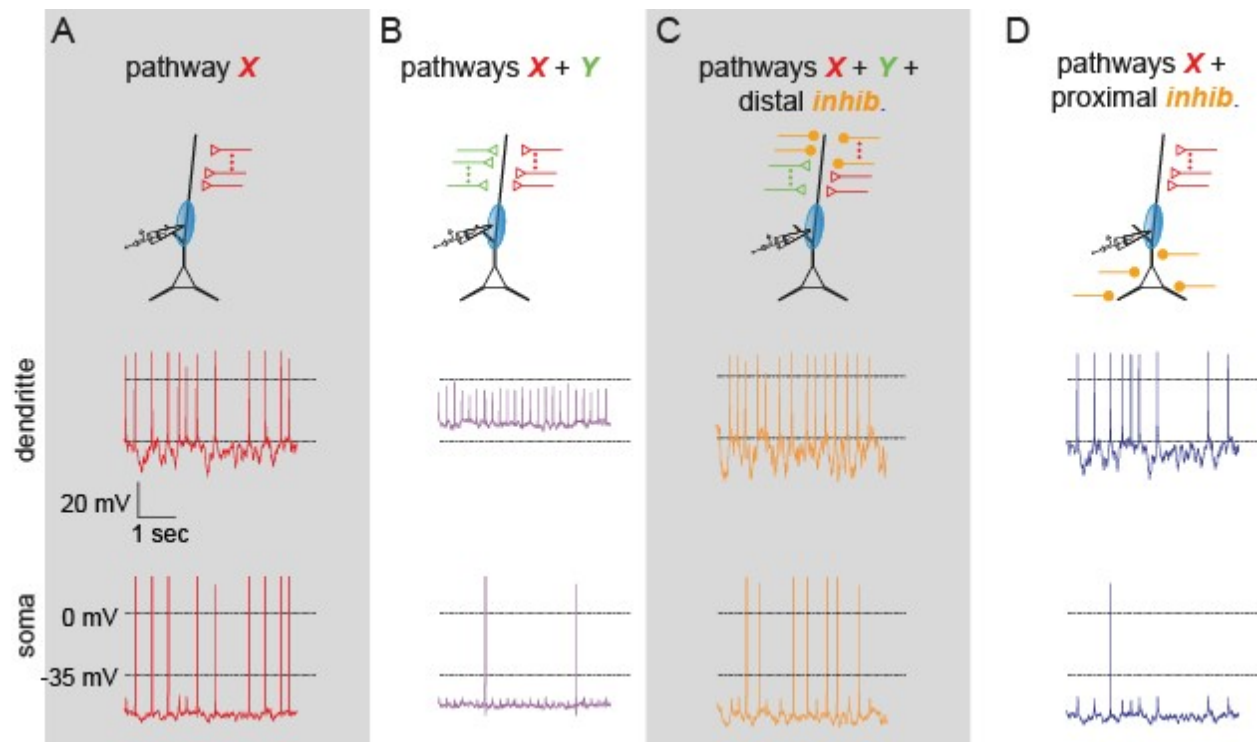
Fig. S9. Combinatorial activation of dCaAPs and somatic APs by the synaptic inputs.
Here we used identical model as in **Fig. 3** (see also **Methods)** but with dCaAP channels located 287 μm from the soma. Current threshold for dCaAPs (I_{rhe}) was 500 pA. **A.** Pathway X with 35 synapses distributed over a subregion of the apical dendrite (as in **Fig 3A**) was able to trigger dCaAPs (top trace) that were coupled with somatic APs (bottom trace). **B.** Pathways $X + Y$ were less effective in triggering APs at the soma because they suppressed the dCaAP amplitudes. **C.** 35 distal inhibitory synapses (≥ 700 μm from the soma, e.g. inhibition from Martinotti cells (*28*)) in addition to pathways X and Y caused dCaAPs to regain their amplitudes and impact on the somatic output. **D.** When pathway X was activated with 35 proximal inhibitory synapses distributed on the basal dendrite (e.g. inhibition from basket cells (*46*)), dCaAP amplitudes were maximal as in A, but firing of APs at the soma was inhibited. Somatic firing rates were 1.7 Hz

(A), 0.54 Hz (B), 1.5 Hz (C), 0.25 Hz (D). All synapses in the model were active at 20 Hz.
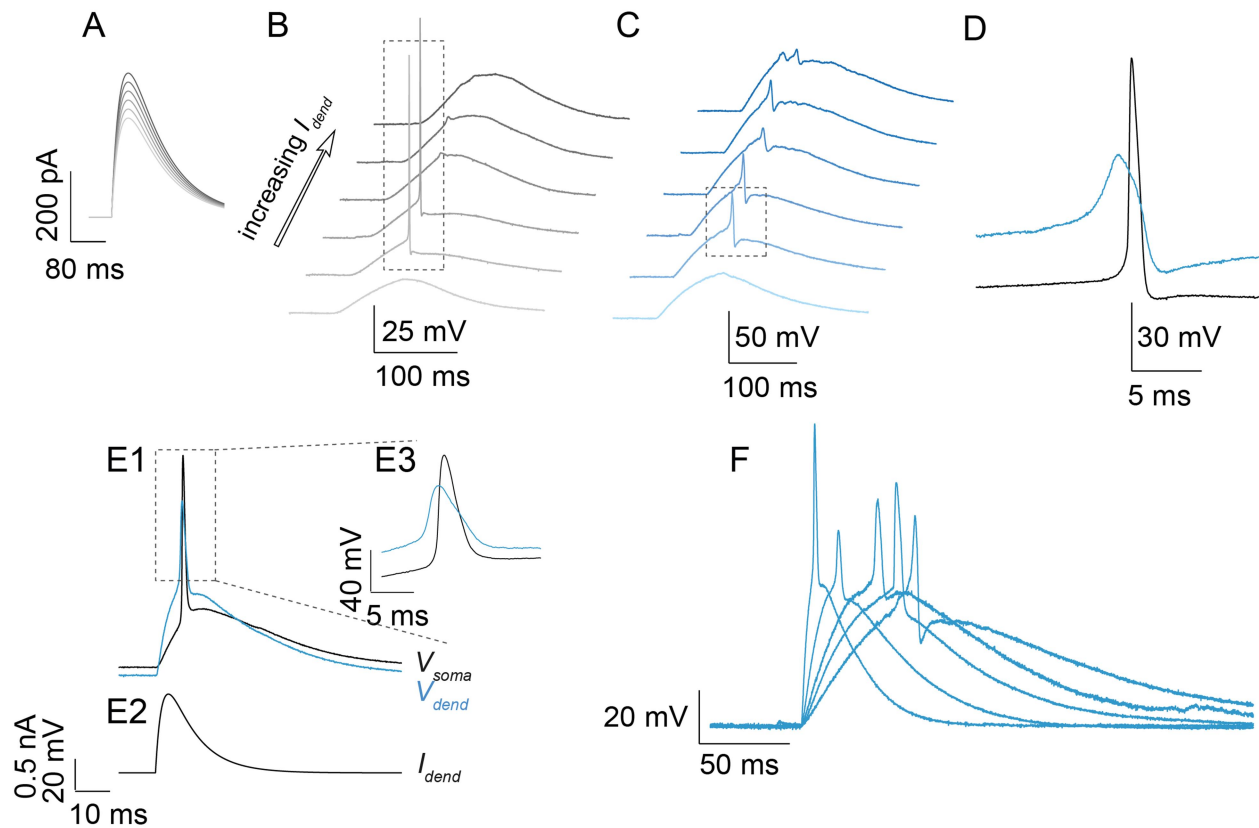
Model files can be downloaded from http://modeldb.yale.edu.

Fig. S10. dCaAP are evoked by transient inputs.

A. I_{dend} injected 260 μm from the cell body, with 20 ms rise time constant and 80 ms decay time constant emulates a transient synaptic barrage to the dendrite. **B-C.** Somatic (B) and dendritic (C) firing as a response for I_{dend} in A. As I_{dend} increased dCaAP amplitude decreased and somatic APs were no longer triggered (top three traces). **D.** Magnified dCaAP (in blue; framed in C) preceded the somatic AP (in black; framed in B). **E.** dCaAP and somatic AP (E1) for I_{dend} with 2 ms rise time constant and 8 ms decay time constant (E2) and magnified dCaAP and somatic AP (E3) for the framed dCaAP in E1. **F.** dCaAPs at threshold in different dendrites for I_{dend} with rise time constant of 2–20 ms and decay time constant of 20–80 ms.
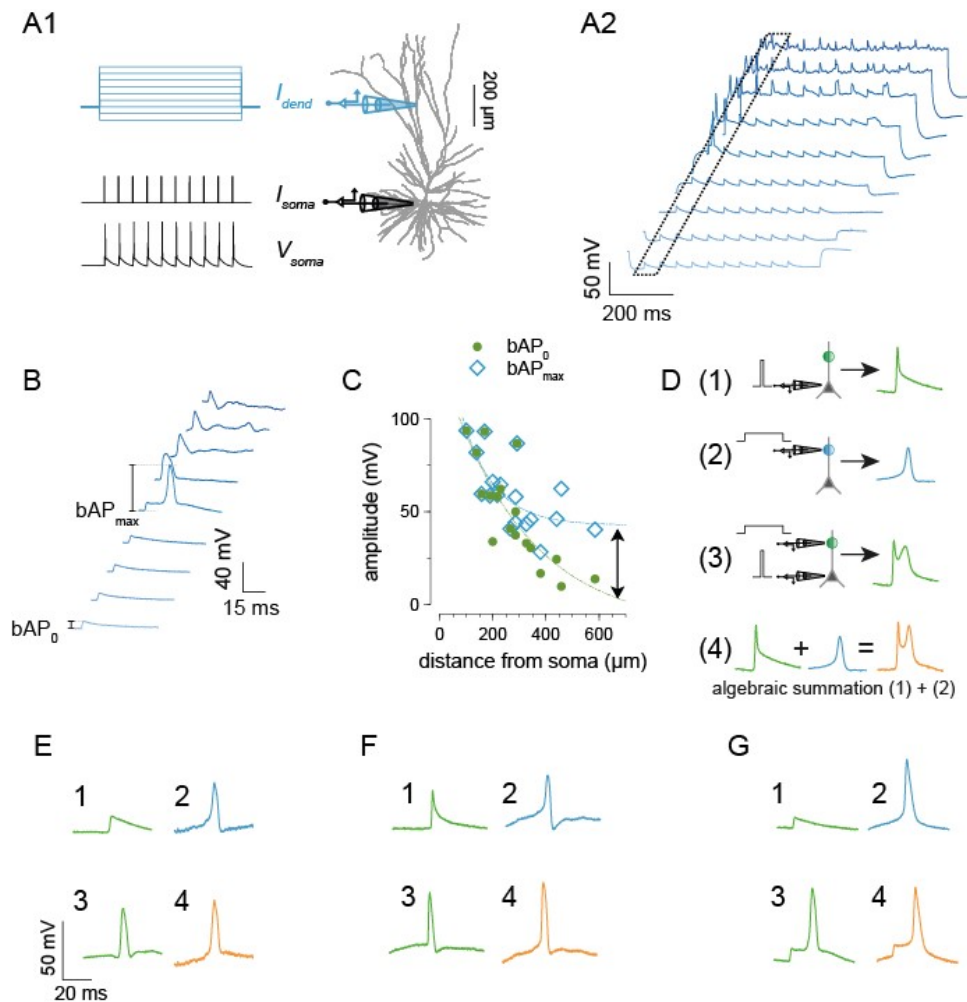
Fig. S11. Non-destructive summation between bAP and dCaAP.

A. Experimental schematic. Stimulus (A1) and recorded voltage traces (A2) for 10 brief pulses

(2 ms each) injected to the soma triggering reliable somatic APs. Step currents with increasing

strength injected into the dendrite. **B**. Magnified region framed in A2 showing bAPs for each

value of I_{dend}. bAP_0 is the amplitude of the bAP at $I_{dend} = -100$ pA. bAP_{max} is the maximal bAP

amplitude (for any I_{dend}). **C.** bAP_0 and bAP_{max} are similar for proximal dendritic sites and diverge

for distal sites (black arrow). **D.** Non-destructive collision of bAPs and dCaAPs: (1) bAP evoked

by a brief somatic current stimulus (I_{soma}). (2) dCaAP evoked by I_{dend}. (3) Collision of a bAP and

a dCaAP due to $I_{soma} + I_{dend}$. (4) Algebraic summation of a bAP (from 1) and a dCaAP (from 2)

recorded separately. **E–G.** Examples of collisions in other dendrites. Numbers 1–4 corresponds

to the conditions in D. The similarity in membrane potential between conditions 3 and 4 suggests

that the summation of bAPs and dCaAPs is not destructive.
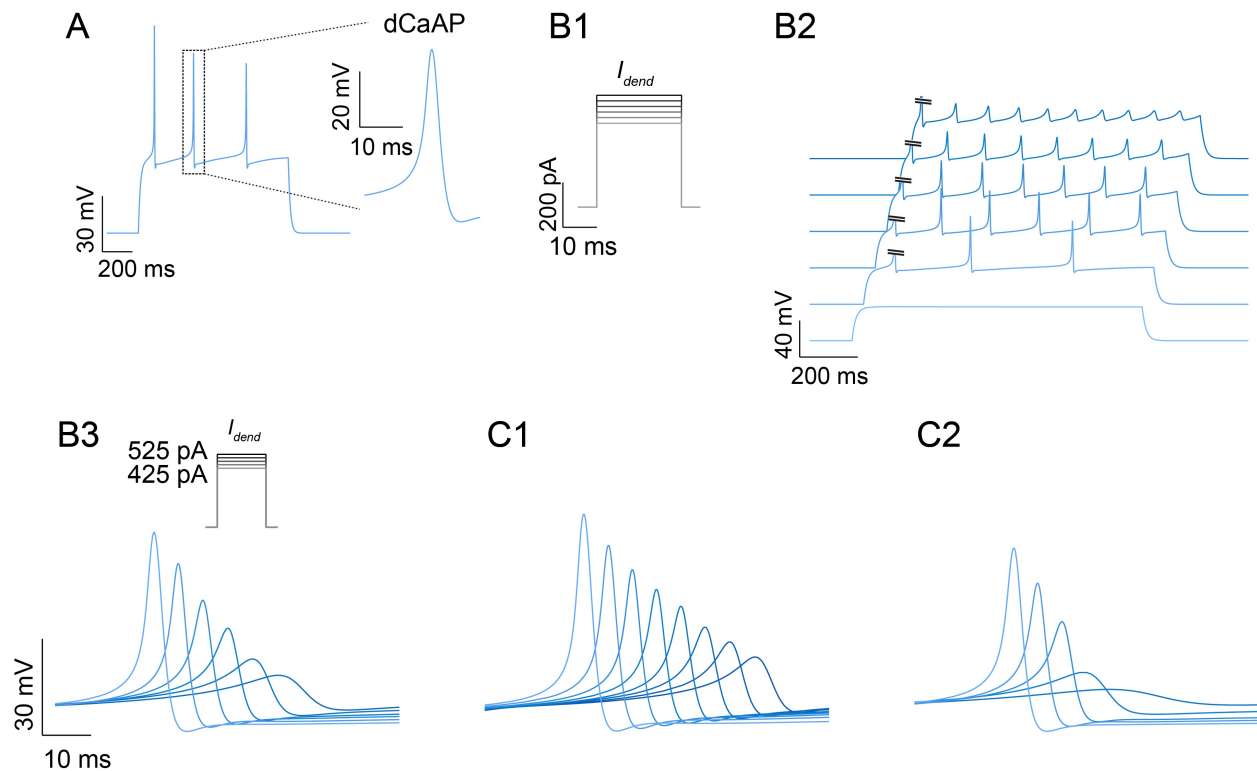
Fig. S12. Modeling dCaAPs with known calcium and potassium channels.

We modeled an isopotential segment of a dendrite in NEURON simulation environment with high voltage Ca^{2+} (HVA-like) channels (*47*), voltage and Ca^{2+} dependent potassium (BK-like) channels (*48*) and leak channels such that R_{in} = 92 MΩ and τ_m = 14 ms. In addition to the functional relevance, BK channels are diverse and know to express in human neurons (*49*). For the intracellular Ca^{2+} ions clearance we used a Ca^{2+} pump from (*50*). Only the time constants of the BK-like channels gates were modified to achieve the characteristic waveform of the dCaAP (**Table S2**; model files can be downloaded from http://modeldb.yale.edu). **A.** Our model faithfully reproduced dCaAPs' amplitude, width and the slow rise time we observed *in vitro*. **B.** As a function of the input (B1) dCaAP amplitude decayed (B2, B3) similar to the results shown in **Fig. 2D**. We could not reproduce this behavior without the Ca^{2+} and voltage dependence of the BK-like channels. For the sake of simplicity we did not use additional mechanism to reduce the

high amplitude of the first dCaAP in each trace as observed *in vitro* (truncated dCaAPs). **C1.** The dCaAPs' decay was weaker than in B3 (as a function of I_{dend}) for faster Ca^{2+} pump time constant (40 ms). **C2** The dCaAPs' decay was stronger than in B3 for slower Ca^{2+} pump time constant. (80 ms ; **Table S2**).

Table S1: Summary of patients' details and diagnosis.

#	Age	Age at epilepsy onset	Sex	Diagnosis	Recent antiepileptic drugs (mg/day)
1	26	19	F	TLE	LTG (500), ZNS (500)
2	29	20	F	TLE	LAC (400), LEV (3000)
3	35	27	M	TLE	LEV (3000), LTG (400)
4	41	25	F	TLE	LTG (400), ZNS (300)
5	32	27	F	TLE	OXC (1500), LEV (3000)
6	54	16	F	TLE	OXC (1200), LTG (200)
7	20	16	F	TLE	LTG (600)
8	42	5	F	TLE	TPM (300), BRV (300)
9	28	13	M	TLE	VPA (2000), OXC (2100)
10	22	12	F	TLE	OXC (1200)
11	18	12	M	TLE	OXC (2400)
12	45	16	M	TLE	ZNS (200), OXC (1200), CLB (10)
13	32	27	M	TLE	LAC (400), LEV (3000), LTG (150)
14	15	–	M	TLE	LEV (2000)
15	26	11	M	MLE	OXC (2100), CLB (20)
16	43	29	M	TLE	LTG (500), LAC (500), CLB (20)
17	36	12	M	TLE	LTG (200), LAC (400)
18	26	14	M	TLE	OXC (1800), TPM (75)
19	31	21	M	TLE	LAC (600), BRV (200)
20	39	1	F	TLE	LTG (300)
21	22	15	M	TLE	LTG (800), ESL (1200)
22	40	26	M	TLE	CBZ (1200), TPM (250), BRV (200)
23	27	10	M	TLE	LAC (400), BRV (50)
24	30	23	M	TLE	LEV (3000),LAC (300),CLB (20)
25	21	14	F	TLE	LTG (900)
26	34	6	M	TLE	LTG (700)
27	21	17	F	TLE	OXC (1000)
28	68	–	M	glioblastoma[1]	
29	63	–	F	glioblastoma[2]	
30	37	–	F	dysembyroplastic neuroepithelial tumor[3]	

M: Male; F: Female; TLE: temporal lobe epilepsy; MLE: multilobar epilepsy;

Antiepileptic drugs specified: BRV: brivaracetam; CBZ: carbamazepine; CLB: clobazam; ESL: eslicarbazepine acetate; LAC: lacosamide; LEV: levetiracetam; LTG: lamotrigine; OXC: oxcarbazepine; TPM: topiramate; VPA: valproate; ZNS: zonisamide;

1. Left frontal region

2. Right temporomesial region and insula

3. Left temporomesial region

Table S2: Summary of main biophysical parameters for the model in Fig. S12.

Channel	Parameter	Value	Modified parameters
BK-like	source	Khaliq et al., (2003)	
	$g_{max}(S/cm^2)$	0.03	
	$\tau_m(ms)$	$\left[0.505 + \dfrac{1000}{(exp((v + 86.4)/10.1) + exp(-(v - 33.3)/10))}\right] \times Fm_\tau$	$Fm_\tau = 5$
	$\tau_h(ms)$	$\left[1.9 + \dfrac{1000}{(exp((v + 48.5)/5.2) + exp(-(v - 54.2)/12.9))}\right] \times Fh_\tau$	$Fh_\tau = 5$
	$\tau_z(ms)$	1	
HVA-like	source	Reuveni et al., (1993)	
	$g_{max}(S/cm^2)$	0.0005	
Ca^{2+} pump	source	Destexhe et al. (1993)	
		$\dfrac{d[Ca]_i}{dt} = -KI_{Ca} - ([Ca]_i - [Ca]_b)/\tau_{Ca}$	$\tau_{Ca} = \begin{cases} 40 \text{ ms, Fig. S12C1} \\ 60 \text{ ms, Fig. S12B3} \\ 80 \text{ ms, Fig. S12C2} \end{cases}$